

# Mass segregation in the outer halo globular cluster Palomar 14

Matthias J. Frank<sup>1,2\*</sup>, Eva K. Grebel<sup>1</sup> and Andreas H. W. Küpper<sup>3,4</sup>

<sup>1</sup> *Astronomisches Rechen-Institut, Zentrum für Astronomie der Universität Heidelberg, Mönchhofstrasse 12 - 14, D-69120 Heidelberg, Germany*

<sup>2</sup> *Landessternwarte, Zentrum für Astronomie der Universität Heidelberg, Königsstuhl 12, D-69117 Heidelberg, Germany*

<sup>3</sup> *Department of Astronomy, Columbia University, 550 West 120th Street, New York, NY 10027, USA*

<sup>4</sup> *Hubble Fellow*

Accepted ????. Received ?????; in original form ?????

## ABSTRACT

We present evidence for mass segregation in the outer-halo globular cluster Palomar 14, which is intuitively unexpected since its present-day two-body relaxation time significantly exceeds the Hubble time. Based on archival Hubble Space Telescope imaging, we analyze the radial dependence of the stellar mass function in the cluster’s inner 39.2 pc in the mass range of  $0.53 \leq m \leq 0.80 M_{\odot}$ , ranging from the main-sequence turn-off down to a  $V$ -band magnitude of 27.1 mag. The mass function at different radii is well approximated by a power law and rises from a shallow slope of  $0.6 \pm 0.2$  in the cluster’s core to a slope of  $1.6 \pm 0.3$  beyond 18.6 pc. This is seemingly in conflict with the finding by Beccari et al. (2011), who interpret the cluster’s non-segregated population of (more massive) blue straggler stars, compared to (less massive) red giants and horizontal branch stars, as evidence that the cluster has not experienced dynamical segregation yet. We discuss how both results can be reconciled. Our findings indicate that the cluster was either primordially mass-segregated and/or used to be significantly more compact in the past. For the latter case, we propose tidal shocks as the mechanism driving the cluster’s expansion, which would imply that Palomar 14 is on a highly eccentric orbit. Conversely, if the cluster formed already extended and with primordial mass segregation, this could support an accretion origin of the cluster.

**Key words:** galaxies: star clusters, stellar dynamics, globular clusters: general, globular clusters: individual: Palomar 14, stars: formation, luminosity function, mass function

## 1 INTRODUCTION

The vast majority of the Galaxy’s globular clusters (GCs) have apparent half-mass two-body relaxation times much shorter than their respective ages (e.g. Harris 1996, 2010 edition). In these clusters, at least in their centers where the density is highest, two-body relaxation has shaped the distribution of stars: in two-body encounters, massive stars tend to lose kinetic energy to lower-mass stars and, as a result, massive stars sink into the cluster’s center, whereas low-mass stars gain energy allowing them to populate orbits further away from the cluster’s center. This is observed as mass segregation, i.e. more massive stars show a more concentrated radial distribution than lower-mass stars. As a consequence, the mass function of the cluster becomes shallower in the cluster center but also globally, as stars at large radii are more easily lost to the Galactic potential (Vesperini & Heg-

gie 1997) and the cluster’s mass-to-light ratio decreases (e.g. Kruijssen & Mieske 2009).

However, in a few GCs, such as the massive clusters NGC 2419 and NGC 5139 ( $\omega$ Cen) and several low-mass, but extended, outer halo clusters, the dynamical half-mass relaxation time  $T_{\text{relax},rh}$  is comparable to or even exceeds the Hubble time. The mass segregation time-scale for a star of mass  $m$  is given  $\langle m \rangle / m \times T_{\text{relax}}$  (Spitzer 1969), where the average stellar mass  $\langle m \rangle$  in GCs is  $\sim 0.2 - 0.3 M_{\odot}$ . Therefore dynamical effects like low-mass star depletion or mass segregation should not have affected the (luminous) main-sequence stars ( $m \sim 0.7 M_{\odot}$ ) in these clusters much, assuming that the cluster parameters such as half-mass radii and cluster masses have not changed dramatically within the last few Gyr and hence that their present-day two-body relaxation times are a representative measure of the relaxation time-scale for their entire lifetime.

One of these clusters is Palomar 14 (Pal 14; also known as AvdB after its discoverers Arp & van den Bergh 1960).

\* E-mail: mfrank@lsw.uni-heidelberg.de

Beccari et al. (2011) recently reported that the distribution of blue straggler stars in Pal 14 is not centrally concentrated with respect to less massive HB and RGB stars in this cluster. Blue stragglers (BS) are hydrogen-burning stars that are brighter and bluer than the main-sequence turn-off of their host population and are believed to form either through direct collisions (Hills & Day 1976) or through mass-transfer in binary systems (McCrea 1964). The radial distributions of BS in massive globular clusters (e.g. Mapelli et al. 2006; Lanzoni et al. 2007) as well as the detection of two distinct sequences of BS in M30 (Ferraro et al. 2009) suggests that both mechanisms are at work in dense GCs. In a diffuse cluster like Pal 14, the low stellar density and therefore low probability of collisions makes it likely that BS are primarily due to mass-transfer in primordial binary systems. Regardless of the formation channel, the masses of BS, or at least the total masses of their progenitor binary systems, likely exceed those of any other single star that can be identified in a cluster’s color-magnitude diagram (e.g. Shara et al. 1997; Geller & Mathieu 2011). Hence, the distribution of BS with respect to lower-mass tracers is widely used as an indicator for mass segregation and the state of dynamical evolution of GCs (e.g. Ferraro et al. 2012). Accordingly, Beccari et al. (2011) interpreted their finding as proof that two-body relaxation has not yet affected Pal 14, not even in its center, and that the cluster is not mass-segregated, in agreement with the expectation from its long present-day half-mass relaxation time of  $\sim 20$  Gyr (Sollima et al. 2011).

Pal 14’s dynamical state has recently also received considerable attention in the context of testing modified Newtonian dynamics (MOND; Milgrom 1983). The cluster’s large Galactocentric distance of  $\sim 66$  kpc (Sollima et al. 2011) in combination with its low mass and density, and therefore the low external and internal acceleration experienced by its stars, make it an excellent test case for this theory (Baumgardt et al. 2005; Sollima & Nipoti 2010; Haghi et al. 2011). In this context, Jordi et al. (2009) measured radial velocities of 16 cluster members and found a good agreement between the cluster’s photometric and dynamical mass in classical Newtonian dynamics. Their measured velocity dispersion is significantly lower than predicted in MOND (Haghi et al. 2009), although MOND cannot be ruled out from these data (Gentile et al. 2010). Küpper & Kroupa (2010) reanalyzed the Jordi et al. (2009) radial velocities including a heuristic treatment of binaries and mass segregation, and argued that Pal 14 has to have a very low binary fraction in order to be compatible with the low observed velocity dispersion. In a Monte-Carlo analysis of the data that included the effects of binaries, of the external field and of velocity anisotropy, Sollima et al. (2012) found that the cluster is compatible with Newtonian dynamics also when the constraint of the binary fraction is relaxed to  $\lesssim 30$  per cent. Tidal tails around the cluster, first detected at low significance in Sloan Digital Sky Survey (SDSS; Abazajian et al. 2009) data by Jordi & Grebel (2010) and confirmed in deeper wide-field imaging by Sollima et al. (2011) may further complicate the interpretation of the small sample of radial velocities as unbound stars may contaminate the sample (e.g. Küpper et al. 2011).

Pal 14 was also the subject of the first full collisional  $N$ -body simulations of a GC over its entire lifetime by Zonoozi et al. (2011). These authors found that, while two-body relaxation does have an effect on the cluster’s stellar mass

function, the effect from two-body relaxation is too weak such that the shallow present-day mass function slope<sup>1</sup> of  $\alpha = 1.3 \pm 0.4$  measured by Jordi et al. (2009) cannot be reproduced with models starting with a Kroupa (2001) initial mass function (IMF). Zonoozi et al. (2011) demonstrated that the observations can, in principle, be reproduced by models with primordial mass segregation, but that the necessary degree of mass segregation has to be very high. Alternatively, they argued that the cluster must have lost a good fraction of its low mass stars in the early gas-expulsion phase, referring to an effect studied by Marks et al. (2008). However, also this latter scenario would require that the cluster must have formed with a high degree of primordial mass segregation. Hence, in any case Pal 14 should be mass-segregated nowadays, since otherwise the observational evidence for a flattened present-day mass function of this cluster is at odds with our current understanding of stellar dynamics or with the assumption of a universal IMF.

In this contribution, we use archival Hubble Space Telescope (*HST*) data reaching down to  $\sim 4$  mag below the main-sequence turn-off to test whether the cluster is mass-segregated in order to shed light on its dynamical state. The paper is structured as follows: we present the observational data we use and describe our data analysis in Section 2. In Section 3 we report our results on the state of mass segregation in Pal 14, followed by a discussion of our findings in Section 4, and we end with a short summary of our work in Section 5.

## 2 OBSERVATIONS AND LITERATURE DATA

Our analysis is based on archival *HST* imaging, obtained with the Wide-Field Planetary Camera 2 (WFPC2) in program GO 6512 (PI: Hesser). The data were first published in the literature by Dotter et al. (2008b) and were also used to measure the slope of the cluster’s overall central mass function by Jordi et al. (2009), who did not attempt quantify mass segregation due to the relatively small WFPC2 field of view. The data consist of F555W ( $V$ ) and F814W ( $I$ ) band images with the cluster approximately centered on the WF3 chip of the camera. With exposure times of  $4 \times 160$  s,  $1 \times 900$  s and  $7 \times 1000$  s (amounting to 8540 s in total) in F555W, and  $4 \times 230$  s,  $4 \times 1100$  s,  $2 \times 1200$  s, and  $2 \times 1300$  s (10320 s in total) in F814W, this is the deepest available imaging of the cluster’s center, reaching out to a radius of 1.9 arcmin, or 39.2 pc (assuming a distance of 71 kpc, see Section 2.2).

The data were reduced in the same way as described in more detail in section 2.3 of Frank et al. (2012). PSF-fitting photometry was obtained using the HSTPHOT package (Dolphin 2000). HSTPHOT was initially run on the individual images and the resulting catalogs were cross-matched in order to refine the image registration. The refined image registration was used for a cosmic ray rejection with HSTPHOT’s crmask task, and as an input for the photometry from all frames using one of the deep F555W frames as reference image. HSTPHOT provides the photometry obtained from each frame, as well as a combined photometric catalog

<sup>1</sup> Throughout this paper, the sign convention is such that positive  $\alpha$  corresponds to negative power-law exponent, i.e. the Salpeter (1955) IMF has a slope of  $\alpha = +2.35$ .

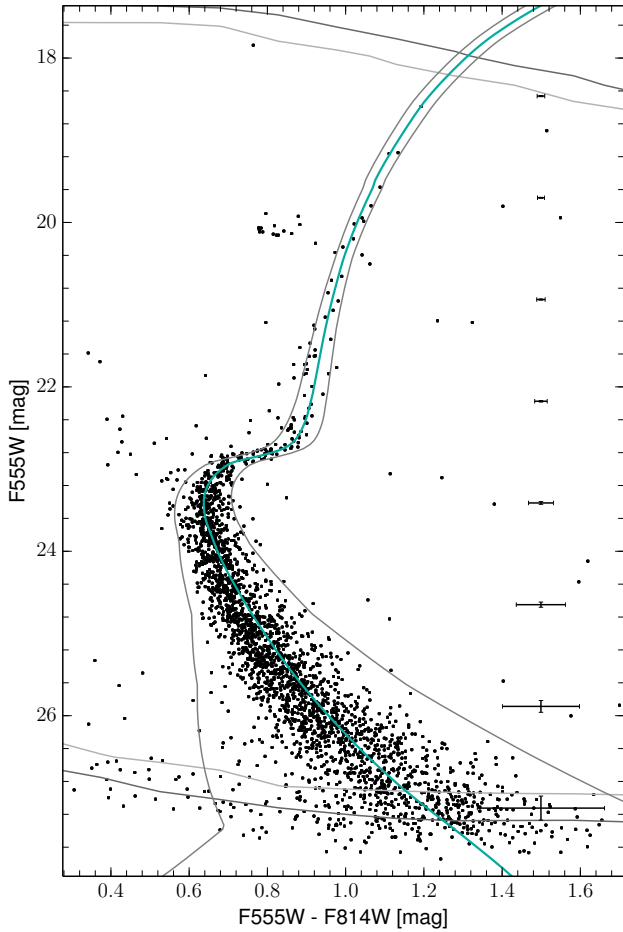


**Figure 1.** Observed color-magnitude diagram of Pal14. Error bars on the right represent the photometric errors derived from artificial star tests. The gray lines at the faint and bright ends represent the 80% (light gray) and 50% (dark gray) completeness contours; at the bright end ( $F555W \lesssim 18$  mag), completeness declines due to saturation even in the shorter exposures. The isochrone, taken from the Dartmouth Stellar Evolution Database (Dotter et al. 2008a) corresponds to an age of 11.5 Gyr,  $[Fe/H] = -1.5$  dex and  $[\alpha/Fe] = +0.2$  dex (see Section 2.2). Gray curves to the left and to the right of the isochrone represent the color limits used for our analysis of the cluster’s mass function.

with average magnitudes for each filter, which we used. The following quality cuts were applied to the resulting all-frames photometric catalog to select clean stellar detections (for details, see the HSTPHOT user manual): a type parameter of 1 (i.e. a stellar detection),  $\text{abs}(\text{sharpness}) < 0.2$ ,  $\chi < 2.0$ , and in both filters a crowding parameter  $< 1.5$  mag and a statistical uncertainty in the magnitude  $< 0.2$  mag. The resulting color-magnitude diagram, containing 3201 stars, is shown in Fig. 1.

HSTPHOT was also used to perform artificial star tests with  $\sim 1.4 \times 10^6$  fake stars in order to estimate the photometric uncertainties and completeness. Artificial stars were distributed homogeneously on the WFPC2 chips (HSTPHOT option 4096) and in the range  $16 \leq V \leq 29$  mag and  $-1.5 \leq (V - I) \leq 4.5$  mag in color-magnitude space. HSTPHOT transforms this into equivalent *HST*-system  $F555W$  and  $F814W$  magnitudes and, while covering the entire grid,

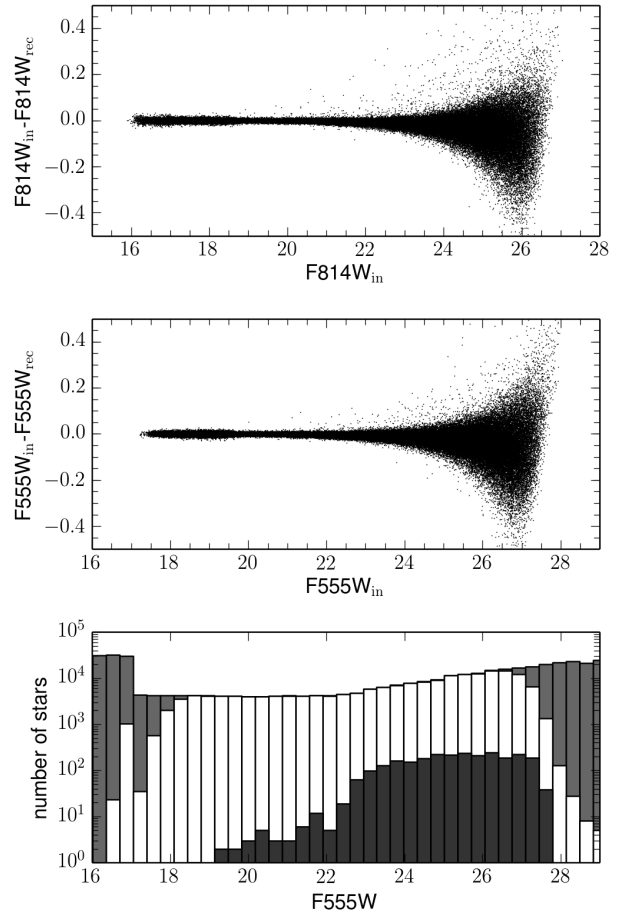


**Figure 2.** The upper two panels show the photometric errors derived from the artificial star tests as a function of magnitude in the  $F814W$  (top panel) and  $F555W$  (middle panel) filter. Shown is the difference between inserted magnitude and recovered magnitude based on  $\sim 200000$  artificial stars that lie within the color selection shown in Fig.1. The lower panel shows the luminosity function in the  $F555W$  filter of observed stars (dark gray histogram), and inserted (light gray) and recovered (white) artificial stars within the color selection, to illustrate that the artificial star tests sample the whole range of magnitudes very well.

generates more artificial stars in regions of the CMD with a high density of observed stars (cf. the HSTPHOT User’s Guide). Since for our subsequent analysis we selected only artificial stars falling close to the isochrone (see below), the exact distribution of inserted artificial stars is unimportant and this mechanism simply yields a more efficient sampling of the relevant color-magnitude regions. The lower panel of Fig. 2, which shows the luminosity functions of observed stars, as well as inserted and recovered fake stars, illustrates that the whole range of observed magnitudes is covered very well by the artificial star tests. HSTPHOT inserts artificial stars into each image using the previously constructed PSF and attempts to re-find the inserted stars and measure their brightness. At any given time, HSTPHOT adds only one single artificial star to all frames and then tests whether this star can be recovered. This procedure avoids self-crowding within the artificial star tests. In HSTPHOT artificial stars are considered detected, if they are found within 3 pixels

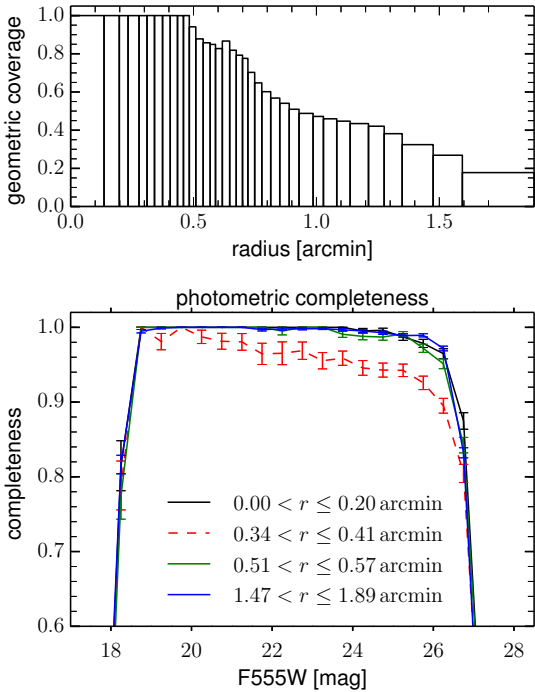


**Figure 3.** Geometric coverage and photometric completeness of the WFPC2 data as a function of radius from the cluster center. The upper panel shows the geometric coverage of our photometric catalog, i.e. the area covered by the WFPC2 pointing in a given radial annulus divided by the total area of that annulus. The annuli were defined to contain each one 36th of the observed stars in our catalog. The lower panel shows the photometric completeness obtained from artificial star tests as a function of F555W magnitude (evaluated in bins of 0.5 mag) in four representative radial ranges. Completeness only marginally varies with radius, indicating that crowding does not strongly affect the photometry in this sparse cluster. There is a dip in completeness at  $r \sim 0.35$  arcmin (red dashed curve) that is caused by a very bright foreground star located at this distance from the cluster center.

(4.5 pixels on the PC chip) of their inserted position and if no other star within that radius dominates the flux at this position (see Holtzman et al. 2006, for a detailed description of the HSTPHOT artificial star procedure). We applied the same quality cuts as used for the observed stars to the resulting artificial star catalog. Photometric uncertainties in a given region of the CMD and on the sky were then estimated from the differences between inserted and recovered magnitudes. Error bars on the right-hand side of Fig. 1 represent the uncertainty in magnitude and color as a function of magnitude for main-sequence and RGB stars. For this and our analysis of the mass-function we used only the subset of  $\sim 200000$  artificial stars that lie within the color selection indicated by the gray lines to both sides of the isochrone in the same figure. These color limits were chosen to exclude stars that deviate in color from the locus of the adopted isochrone (see Section 2.2) by more than  $3\sigma_{\text{col}}$ , where  $\sigma_{\text{col}}$  is the color uncertainty derived from the artificial star results in the corresponding region of the CMD. The upper two panels of Fig. 2 show the distribution of photometric errors (i.e. inserted-recovered magnitude) as a function of

magnitude in both filters derived from artificial stars that fall within the color selection around the isochrone.

The photometric completeness was estimated from the ratio of the number of recovered to the number of inserted artificial stars. The completeness, within the color selection, as a function of F555W magnitude, at four different distances from the cluster center, is shown in the lower panel of Fig. 3. It is apparent that crowding does not or only marginally affect the photometry, as the completeness is essentially independent of the distance from the cluster center, apart from a dip in completeness at  $\sim 0.35$  arcmin that is caused by a bright foreground star in the field.

The geometric coverage of the WFPC2 photometry, shown in the upper panel of Fig. 3, was quantified as the ratio of the area of covered pixels in a given radial annulus around the cluster’s center to the total area of that annulus. The covered pixels were selected on a distortion-corrected frame combined with MULTIDRIZZLE (Koekemoer et al. 2006) by the requirement that the covered pixels receive at least 25 per cent of the total exposure time in both filters and be included in the reference frame used for photometry (see Frank et al. 2012). The stellar positions in the photometric and artificial star catalogs were transformed to the coordinate system of the distortion-corrected, drizzled frame and stars falling on pixels marked as ‘not covered’ were removed from both catalogs to avoid border effects. For the cluster’s center, we used the coordinates determined by Hilker (2006), which agree within the uncertainties with the center determined by Beccari et al. (2011). Since the absolute astrometric accuracy of the *HST* is limited by the accuracy of its guide star catalog, we registered the distortion-corrected coordinate frame to the SDSS DR7 catalog (Abazajian et al. 2009), before transforming the coordinates of the center to pixel coordinates in our photometric catalog.

## 2.1 Foreground contamination

Since the WFPC2 photometry covers only the inner region of the cluster and no nearby comparison fields are available, we used the Besançon model of the Galaxy (Robin et al. 2003) to estimate the expected contamination by foreground stars in our field. We queried the model for stars out to 200 kpc in the direction of Pal 14. For better number statistics, we used a solid angle of 50 square degrees and the model’s ‘small field’ mode that simulates all stars in the same line of sight, so that any spatial variation in the foreground that could be present in such a large field is neglected. The remaining model parameters, such as the extinction law and spectral type coverage, were kept at their default values.

We transformed the  $V$  and  $I$  magnitudes of the resulting synthetic foreground catalog to F555W and F814W magnitudes by inverting the Holtzman et al. (1995) WFPC2 filter to  $UBVRI$  transformations. The photometric uncertainties and completeness derived from artificial star tests were imposed on the foreground catalog using the procedure described in more detail in Frank et al. (2012). The radial variation of these properties was taken into account by assuming the foreground stars to be distributed homogeneously over the sky and performing the procedure on radial sub-samples of artificial and foreground stars.

The left panel of Fig. 4 shows the density of foreground stars in our pointing, evaluated in bins of 0.25 mag in F555W

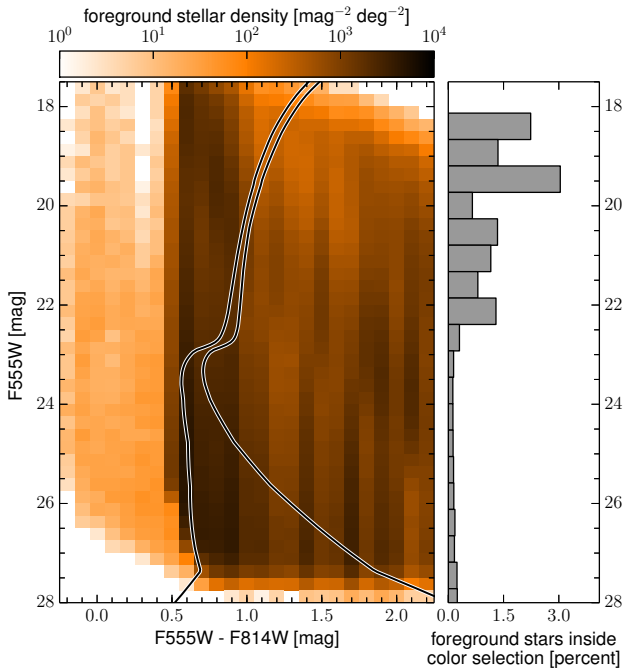


**Figure 4.** The left panel shows the density of foreground stars in the color-magnitude diagram. The photometric uncertainties and completeness inferred from artificial star tests were imposed on the Besançon foreground catalog. The density of foreground stars was evaluated in bins of 0.25 mag in F555W and 0.1 mag in color. The color scale indicates the density in units of foreground stars per square magnitude in the CMD and square degree on the sky. Black-on-white lines correspond to the region of the CMD used to estimate the mass function of Pal 14. Within these color limits, the fraction of expected contaminants in the photometric catalog, averaged over 0.5 mag in F555W is shown in the right-hand panel. The fraction is well below 1 per cent on the main sequence and up to 3 per cent on the sparsely populated RGB.

and 0.1 mag in color and scaled to units of stars per mag in color and magnitude in the CMD and per square degree on the sky. Given the small effective area of the WFPC2 pointing of 4.72 square arcmin the number of expected foreground stars in our catalog is low. The ratio of expected foreground stars to observed stars inside our color selection, averaged over bins of 0.5 mag in F555W, is below  $\lesssim 3$  percent over the whole range of luminosities and even lower on the main sequence, as shown in the right-hand panel of Fig. 4. Therefore, we chose to not correct the main-sequence star counts for foreground stars.

## 2.2 Adopted stellar population parameters

In Section 3.2 we will use an isochrone as a relation between stellar magnitude and mass, and thus require the knowledge of the distance, reddening, age and chemical composition of the cluster. There are two photometric studies of the cluster’s population parameters based on the same WFPC2 data we use here. Dotter et al. (2008b) analyzed the photometry transformed to the Johnson-Cousins  $V$  and  $I$  filters, and applied offsets in the  $V$  and  $I$  zeropoints to match the ground-based standard star photometry of Stetson (2000). In this system, they obtained a best-fitting Dartmouth

isochrone (Dotter et al. 2008a) for a distance of 79 kpc with  $[\text{Fe}/\text{H}] = -1.5$  dex,  $[\alpha/\text{Fe}] = +0.2$  dex and an age of 10.5 Gyr. Jordi et al. (2009) used the WFPC2 instrumental magnitudes and the same library of Dartmouth isochrones and adopted the spectroscopic metallicity of  $[\text{Fe}/\text{H}] = -1.5$  dex from Harris (1996), which in turn is based on measurements by Zinn (1985) and Armandroff et al. (1992). They found a best-fitting isochrone with  $[\alpha/\text{Fe}] = +0.2$  dex, an age of  $11.5 \pm 0.5$  Gyr, and a distance of  $71 \pm 1.3$  kpc.

From ground-based photometry, Hilker (2006) derived an age of 10 Gyr,  $[\text{Fe}/\text{H}] = -1.5$  dex,  $[\alpha/\text{Fe}] = +0.3$  dex and a distance of 77 kpc based on Yonsei-Yale isochrones (Kim et al. 2002). Sollima et al. (2011) adopted  $[\text{Fe}/\text{H}] = -1.6$  dex and  $[\alpha/\text{Fe}] = +0.3$  dex and found a distance of  $71 \pm 2$  kpc as well as an older age of  $13.2 \pm 0.3$  Gyr based on Padova isochrones (Marigo et al. 2008). While this age seems at odds with differential age dating, which suggests that Pal 14 is several Gyr younger than classical old GCs (Sarajedini 1997; Dotter et al. 2008b), differences in the absolute age may also stem from differences in the ‘age scale’ of different sets of isochrones (see e.g. Glatt et al. 2008; Marín-Franch et al. 2009).

Finally, from high-resolution spectroscopy of red giants, Çalışkan et al. (2012) recently derived a metallicity of  $[\text{Fe}/\text{H}] = -1.3$  dex (the mean of their  $[\text{FeI}/\text{H}]$  and  $[\text{FeII}/\text{H}]$  values) and  $[\alpha/\text{Fe}] = +0.3 \pm 0.2$  dex.

For our analysis in the WFPC2 instrumental magnitude system, we adopt the parameters derived by Jordi et al. (2009) in this system and specifically also their reddening of  $E(\text{F555W} - \text{F814W}) = 0.063$  mag as well as their derived apparent distance modulus of  $(m - M)_{\text{F555W}} = 19.45$  mag. The adopted values are well within the scatter of parameters found by other authors, but we keep in mind that there is some scatter, even when the parameters are derived from the same data and with the same set of isochrones. We will discuss the influence of these uncertainties on the mass function in Section 3.4.

## 3 RESULTS

### 3.1 Luminosity function in the center and outer region

As a first diagnostic for the presence of mass segregation, we show in the upper panel of Fig. 5 the luminosity functions of stars falling into the color selection shown in Fig. 1 in the innermost and outermost regions covered by our catalog. The central region, represented by the gray thick histogram, was defined as  $r < 0.3$  arcmin, in order to avoid the region around the bright foreground star at  $r \sim 0.35$  arcmin (see the lower panel of Fig. 3). The outer region (thin black line) was defined as  $r > 1$  arcmin, where, as we will see in the next Section, the mass function appears to start to steepen. It is apparent that both the central and the outer sample contain a similar number of stars around 23 mag in F555W, just above the main-sequence turn-off (23.4 mag). At fainter magnitudes, however, the luminosity function in the outer region appears to be more populated than in the central region, indicating the presence of mass segregation. The upper panel of Fig. 5 also shows the luminosity functions corrected for photometric incompleteness as thick gray and thin black

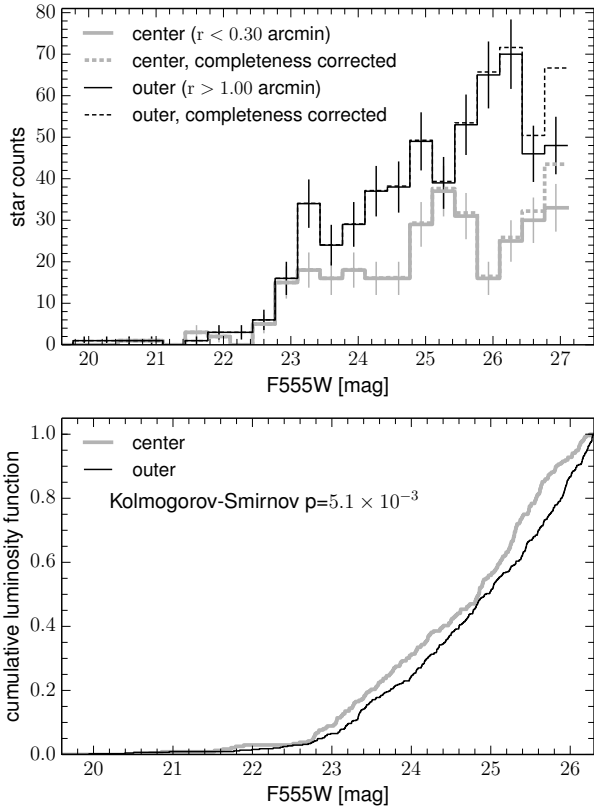


**Figure 5.** The upper panel shows the observed luminosity functions in bins of  $1/3$  mag in F555W for stars inside the color selection shown in Fig. 5 in the center (thick gray lines;  $r < 0.3$  arcmin) and the outer region covered by our catalog (thin black lines;  $1 < r < 1.9$  arcmin). The dashed gray and black lines correspond to the luminosity functions corrected for photometric incompleteness and expected foreground stars. It can be seen that while both samples contain similar numbers of stars around  $\sim 23$  mag, just above the main-sequence turn-off, the outer sample contains more faint stars than the central region. The lower panel shows the cumulative luminosity distribution functions of observed stars brighter than 26.3 mag in the central and outer region, where both samples are approximately complete. A Kolmogorov-Smirnov test yields a probability of 0.5 per cent that the two samples are drawn from the same luminosity distribution.

dashed lines for the central and outer regions, respectively. The completeness corrections were estimated from the ratio of recovered to inserted artificial stars inside the color selection shown in Fig. 1 in the inner and outer region. They thus represent a crude overall completeness correction in the respective radial ranges; in the analysis in the following Section, a more precise, *local* correction for photometric incompleteness and geometric coverage will be applied. We also calculated the luminosity function of foreground stars expected according to the Besançon model from Section 2.1 within the effective areas covered by the central and outer samples, of  $0.3 \text{ arcmin}^2$  and  $2.34 \text{ arcmin}^2$ , respectively. As already expected from the right-hand panel of Fig. 4, the number of predicted foreground contaminants is very low. Their F555W luminosity function in the outer (inner) region rises almost monotonically from 0.006 (0.0008) stars per 0.33 mag bin at 18.6 mag, to 0.2 (0.02) stars per bin

at 26.9 mag. Compared to the number of observed stars the contamination is therefore negligible and was not subtracted from the observed luminosity function.

In order to quantify the apparent difference of the two luminosity functions shown in the upper panel of Fig. 5, we used a two-sided, two-sample Kolmogorov-Smirnov test to compare the cumulative (unbinned and not completeness-corrected) luminosity functions in both samples. For this, we used only stars brighter than 26.3 mag, since these are largely unaffected by photometric incompleteness. The cumulative distribution functions are shown in the lower panel of Fig. 5. The Kolmogorov-Smirnov test yields a probability of only 0.5 per cent that the observed luminosity functions of the central and outer region stem from the same underlying distribution.

### 3.2 Mass segregation

We determined the stellar mass function in the cluster in the mass range  $0.53 \leq m \leq 0.80 M_{\odot}$ , corresponding to stars fainter than the main-sequence turn-off with  $23.4 \text{ mag} \lesssim \text{F555W} \lesssim 27.1 \text{ mag}$ , inside the color selection that is shown in Fig. 1 and defined in Section 2. Photometric completeness, which decreases at the faint end, is still  $\gtrsim 70$  per cent in the lowest mass bin at all radii. The color selection removed likely foreground stars and blue stragglers. To each of the selected stars, we assigned a mass based on the adopted isochrone by interpolating the magnitude-mass relation defined by the isochrone to the star's measured F555W magnitude.

While the photometric completeness only marginally varies with distance from the cluster center, both the geometric coverage and the stellar density do vary as a function of radius (Fig. 3). Since we are interested in the mass function within a given radial range in the cluster, rather than in our catalog, it is necessary to apply a radially varying correction to the number of observed stars to ensure a correct weighting when combining stars from different radii to calculate the mass function. Correcting for the missing area in a given radial annulus necessarily has to assume that the cluster's stellar distribution is axially symmetric around the center. This is justified, given that a distortion of the isophotes that marks the onset of the tidal tails is visible only at radii  $\gtrsim 5$  arcmin (Sollima et al. 2011; Beccari et al. 2011), while our catalog extends out to only 1.9 arcmin. We divided our photometric catalog into  $n$  radial bins around the cluster center, and for each bin calculated the corrections for missing area and for photometric completeness as a function of F555W magnitude (see Fig. 3). The bins were chosen such that each of them contained one  $n$ th of the observed stars, optimal in terms of the Poissonian uncertainties of the star counts.  $n$  has to be large enough to capture the variation of the geometric coverage and stellar density with radius, but should not be chosen larger than necessary to avoid statistical fluctuations caused by low numbers of artificial stars in the individual radial bins. We chose  $n = 36$  bins for our analysis after verifying that increasing the number of subdivisions further did not influence any more the derived overall mass function or the integrated stellar mass within 1.9 arcmin.

With only 2120 observed stars within the color selection and the magnitude limits reported above, the mass function

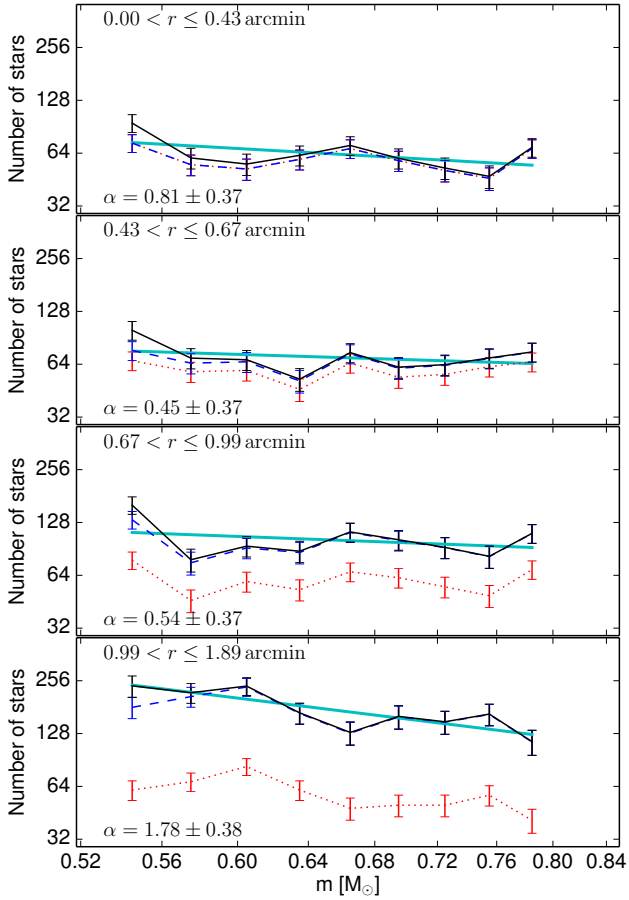


**Figure 6.** The mass function in radial bins containing one fourth of the observed stars each; the radial ranges are reported at the top of each panel. Red dotted lines correspond to the raw star counts, blue dashed lines to the star counts after correction for geometric coverage and black lines to the star counts additionally corrected for photometric incompleteness. The best-fitting power-law mass function, obtained with the maximum-likelihood scheme described in the text is shown as cyan line. The best-fitting mass function slope  $\alpha$  and its  $1\sigma$  uncertainty is reported at the bottom of each panel. In all radial ranges, the mass function is well reproduced by a power-law and its slope is significantly shallower than a Kroupa (2001) mass function in this range of masses ( $\alpha = 2.3$ ).

in the individual 36 radial bins (containing  $\sim 59$  stars each) is poorly constrained. We therefore re-combined several of these bins after the correction for geometric coverage and photometric completeness and measured the mass function.

In the combined radial bins, we sorted stars by mass into 9 mass bins with a width of  $0.03 M_{\odot}$  and fitted the resulting histograms with a power-law of the form  $dN/dm \propto m^{-\alpha}$ . It is common practice and well justified in the case of large number counts  $n_i$ , to treat their uncertainties as Gaussian with dispersions of  $\sqrt{n_i}$ . In this case, a maximum likelihood fit is obtained by minimizing  $\chi^2$  or, equivalently, by maximizing the log-likelihood function

$$\ln \mathcal{L} = k - \sum_{i=1}^N \frac{(f_i - n_i c_i^{-1})^2}{2 (\sigma_i c_i^{-1})^2},$$

where  $k$  is a constant,  $f_i = \int_{m_i}^{m_{i+1}} dN$  is the model predic-

**Table 1.** Observed and completeness corrected mass function in four radial ranges as shown in Fig. 6. Listed are the mass bin center  $M$ , the number of observed stars  $N_{\text{obs}}$ , the geometric coverage correction  $f_{\text{geo}}$ , the photometric completeness  $f_{\text{phot}}$ , and the number of stars corrected for geometric and photometric completeness  $N_{\text{calc}}$ .

$M [M_{\odot}]$	$N_{\text{obs}}$	$f_{\text{geo}}$	$f_{\text{phot}}$	$N_{\text{calc}}$
0.00 < $r$ <= 0.43 arcmin				
0.54	73	1.00	0.77	94.9
0.57	55	1.00	0.92	60.1
0.60	52	1.00	0.94	55.5
0.63	59	1.00	0.95	62.2
0.66	68	1.00	0.96	70.8
0.69	58	1.00	0.97	59.8
0.72	51	1.00	0.97	52.7
0.75	46	1.00	0.98	47.2
0.78	68	1.00	0.99	69.0
0.43 < $r$ <= 0.67 arcmin				
0.54	67	0.87	0.77	99.9
0.57	58	0.89	0.94	69.4
0.60	59	0.89	0.97	67.9
0.63	46	0.89	0.98	52.6
0.66	65	0.89	0.99	74.5
0.69	54	0.89	0.99	61.6
0.72	56	0.89	0.99	63.6
0.75	62	0.90	0.99	69.5
0.78	66	0.88	1.00	75.2
0.67 < $r$ <= 0.99 arcmin				
0.54	78	0.59	0.83	160.7
0.57	46	0.61	0.96	78.5
0.60	59	0.64	0.98	93.8
0.63	53	0.61	0.98	87.8
0.66	67	0.60	0.99	113.1
0.69	62	0.61	0.99	102.0
0.72	55	0.60	1.00	92.3
0.75	49	0.60	1.00	82.1
0.78	69	0.62	1.00	111.0
0.99 < $r$ <= 1.89 arcmin				
0.54	61	0.34	0.75	239.3
0.57	68	0.33	0.95	218.8
0.60	83	0.35	0.99	238.6
0.63	61	0.37	0.99	168.0
0.66	48	0.37	0.99	129.9
0.69	50	0.31	0.99	160.4
0.72	50	0.34	1.00	149.4
0.75	57	0.35	1.00	165.3
0.78	41	0.36	1.00	115.1

tion in the  $i$ -th mass-bin (ranging from mass  $m_i$  to  $m_{i+1}$ ),  $\sigma_i = \sqrt{n_i}$  is the uncertainty of the observed number of stars  $n_i$  and  $c_i$  is the completeness (photometric and geometric) in the given bin. It is also well-known that the Poissonian nature of number counts has to be taken into account in the case of small numbers (e.g. Mighell 1999). Therefore, we chose to maximize the Poissonian log-likelihood function

$$\ln \mathcal{L} = - \sum_{i=1}^N \ln \left( \frac{(f_i c_i)^{n_i} \exp(-f_i c_i)}{n_i!} \right),$$

where the completeness correction has been multiplied into the model term instead of divided into the  $n_i$ . Because of the large number of  $\sim 200000$  artificial stars, the statistical

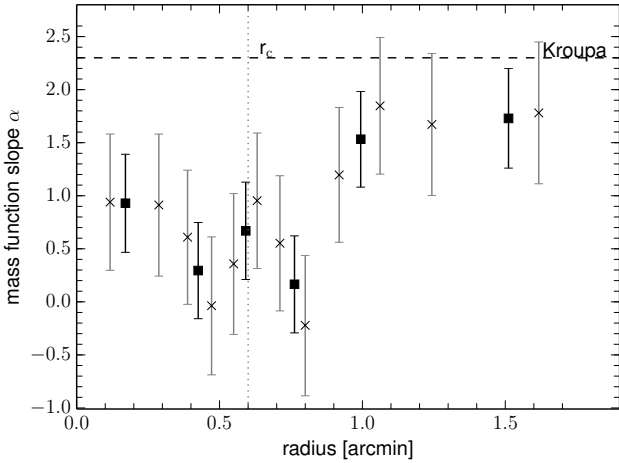


**Figure 7.** The best-fitting mass function slope and its uncertainties in six (black squares) and alternatively in 12 (gray crosses) statistically independent radial bins containing equal numbers (354, or 177, respectively) of observed stars. The radii of the data points correspond to the mean radius in the corresponding radial bin. The cluster’s core radius  $r_c = 0.6$  arcmin, or 12.4 pc (Solima et al. 2011) is indicated by the dotted line. The increase of the mass function slope  $\alpha$  with increasing radius is obvious, although the slope stays below the Kroupa (2001) value of  $\alpha = 2.3$  in this range of masses (shown as dashed horizontal line) out to the maximum radius covered by the WFPC2 photometry.

uncertainty of the completeness is  $\ll 1$  per cent in most radial and mass bins and never exceeds 2.5 per cent, and is therefore negligible compared to that of the observed star counts.

There are several methods to estimate confidence intervals from the likelihood function; one of them is the likelihood ratio method (e.g. Hudson 1971), which we used here: given the maximum likelihood, the  $p$  percent confidence interval for  $k$  parameters of interest is defined as the contour in parameter space, where the likelihood function has dropped by a factor of  $\exp(-Q_{\chi^2_k}(p)/2)$  with respect to its maximum. Here  $Q_{\chi^2_k}(p)$  is the quantile function of the  $\chi^2$  distribution for  $k$  degrees of freedom; for one parameter of interest, the 68.3 percent (or  $1\sigma$ ) confidence interval is given by a decrease in the likelihood by a factor of  $\exp(-1/2)$ . The confidence limits derived in this way in principle need not be symmetric around the maximum likelihood solution. Nevertheless, our calculated upper and lower uncertainties on  $\alpha$  are almost identical, indicating that the likelihood function is symmetric around its maximum. This is also supported by the fact that the results and uncertainties obtained with this Poissonian maximum likelihood fitting did not significantly differ from those obtained for comparison via a common  $\chi^2$ -minimization, despite the low number counts.

The amount of radial sub-divisions is clearly a trade-off between signal-to-noise ratio and radial resolution and we present two realizations of the binning. Fig. 6 shows the mass distributions of observed stars (red dotted lines), the distributions corrected for missing area (blue dashed lines) and the distributions additionally corrected for photometric completeness (black solid lines), as well as the best-fitting power-law mass function, in radial ranges containing each

one fourth of the observed stars (i.e. combining blocks of 9 of the 36 original radial bins). The observed and completeness-corrected mass function in these ranges are also reported in Table 1. From Fig. 6, it can be seen that the mass function in each radial interval is well-reproduced by a single power-law with a slope shallower than a Kroupa (2001) mass function. Moreover, the slope  $\alpha$  in the outer-most radial range ( $1 < r \leq 1.9$  arcmin, corresponding to  $20.7 < r \leq 39.2$  pc) is significantly steeper than in the inner two bins.

The increase of  $\alpha$  with increasing radius is more clearly seen in the finer radial samplings in Fig. 7, which shows the best-fitting mass function slope  $\alpha$  as a function of radius for statistically independent bins containing one sixth of observed stars (black squares), and alternatively containing one 12th of observed stars (gray crosses). To quantify the radial dependence of  $\alpha$ , we fitted different possible models to the data shown as gray crosses in Fig. 7: a constant, a linear relation, a bimodal relation (i.e. a piece-wise constant function with one discrete change), as well as a quadratic relation between radius and  $\alpha$ . We used standard  $\chi^2$  minimization, i.e. assuming that the uncertainties on each  $\alpha$  measurement are Gaussian, which is supported by the symmetry of the likelihood functions found around the best-fitting  $\alpha$  values, as reported above. The functional form and best-fitting parameters for each model are listed in Table 2. It is trivial that a model with more free parameters reproduces the fitted data more closely. On the other hand a, potentially over-fitted model with more free parameters also will do worse in predicting unknown data. Thus, in order to quantify the relative odds of the different models, we use Jackknife, or leave-one-out, cross-validation (e.g. Rust et al. 1995): for each model  $m$ , each of the twelve data points is left out in turn, the maximum-likelihood parameters are determined from the remaining eleven data points. The likelihood  $L_{m,\{i\}}$  of the left-out data point  $i$  given this best-fitting relation is then evaluated. The cross-validated pseudo-likelihood for model  $m$  is then

$$L_m^{CV} = \prod_{i=1}^{12} L_{m,\{i\}}.$$

Under the implicit assumptions of equal prior probabilities for all models and that the true model is contained in the set of examined models, the relative probability for model  $M$  is then

$$p_M = L_M^{CV} \left( \sum_m^{(\text{models})} L_m^{CV} \right)^{-1}.$$

From the relative probabilities, which are reported in the last column of Table 2, the data favor a bimodal relation (with a probability of 88.3 per cent). The data also allow for a linear rise of  $\alpha$  with radius (10 per cent), and suggest that a quadratic relation ( $< 0.1$  per cent), and a constant relation, although less significantly (1.7 per cent) can be excluded.

The apparent steepening (either discrete or continuous) of the mass function as a function of radius indicates that mass segregation is present in Pal 14. Moreover, Fig. 7 shows that the mass function at the outermost radii covered by our photometry is almost compatible with a Kroupa IMF ( $\alpha = 2.3$  in this mass range); since it is likely that the relative abundance of low-mass stars increases further with increasing radius, this suggests that there is no need to invoke

**Table 2.** Functional form of  $\alpha(r)$  fitted to the data points shown as gray crosses in Fig. 7. For each model, the number of free parameters, the functional form with best-fitting parameters and the relative probability of the model are given.

model	parameters	functional form	relative probability
constant	1	$\alpha(r) = 0.9 \pm 0.2$	0.0171
linear	2	$\alpha(r) = (0.2 \pm 0.4) + r \times (0.9 \pm 0.5)\text{arcmin}^{-1}$	0.0996
quadratic	3	$\alpha(r) = (0.8 \pm 0.7) + r \times (0.9 \pm 1.7)\text{arcmin}^{-1} + r^2 \times (1.1 \pm 1.0)\text{arcmin}^{-2}$	0.0004
bimodal	3	$\alpha(r) = (0.5 \pm 0.2)(r \leq 0.86 \pm 0.05), 1.6 \pm 0.3(r > 0.86 \pm 0.05)$	0.8828

a deviation from a universal IMF in this cluster (cf. Zonoozi et al. 2011).

### 3.3 Overall mass function

The overall mass function slope of stars within 1.9 arcmin (i.e. subsuming the star counts from all radial bins) is  $\alpha = 1.1 \pm 0.2$ . This is somewhat shallower than the value of  $\alpha = 1.3 \pm 0.4$  derived by Jordi et al. (2009) from the same data. Although consistent within the uncertainties, the difference is, at first glance, surprising, as we also adopted the best-fitting isochrone from Jordi et al. (2009) in our analysis. The difference can be traced back to a difference in the completeness correction: we calculated the completeness based solely on artificial stars inside the color selection used for the observed stars. If we instead calculated the completeness from the entire artificial star catalog, we would obtain a larger completeness correction in the lowest mass bins, similar to the values given in table 3 of Jordi et al. (2009). However, as can be seen from the completeness contours in the CMD (Fig. 1), for faint stars bluer than the cluster’s main sequence, detection is limited by the F814W filter. Therefore, the inclusion of artificial stars in that region of the CMD would result in an over-correction for completeness.

### 3.4 Systematics in the measurement of the mass function

#### 3.4.1 Dependence on the adopted isochrone

To estimate the systematic effects of the adopted stellar population parameters on the inferred mass function, we measured the mass function using the same ‘measurement’ isochrone as before from an artificial luminosity distribution that was generated based on the assumption that the cluster’s actual stellar population parameters are different. For this experiment we chose an ‘input’ isochrone from the (Dotter et al. 2008a) data base that differed in age,  $[\text{Fe}/\text{H}]$ , or  $[\alpha/\text{Fe}]$  from our adopted values. We then drew 2000 stars in the range of  $0.53 - 0.80 M_{\odot}$  from a power-law mass function with slope  $\alpha_{\text{in}}$  and converted the masses to a luminosity distribution according to this input isochrone.

The location of the main-sequence turn-off of the input isochrone in general differed from that of the measurement isochrone. However, any isochrone advocated as the best-fitting isochrone in an observational study will be one that reasonably well reproduces the cluster’s main-sequence turn-off. Therefore, we shifted our measurement isochrone in magnitude and color such that its turn-off point coincided with the insertion isochrone. In observations, these shifts

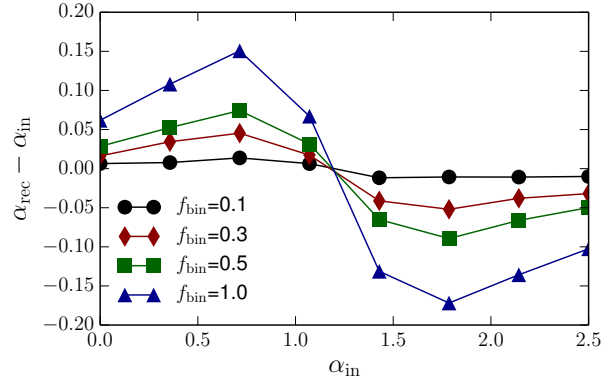


**Figure 8.** The influence of unresolved binaries on the measured mass function slope. The difference of recovered  $\alpha_{\text{rec}}$  and inserted  $\alpha_{\text{in}}$  is shown as a function of  $\alpha_{\text{in}}$  based on simulations (see text) including a varying fraction of binaries,  $f_{\text{bin}}$  ranging from 0.1 to 1 and represented by different symbols. For realistic binary fractions of  $f_{\text{bin}} \lesssim 0.5$ , the impact of randomly paired binaries is relatively small, with a maximum systematic uncertainty in  $\alpha$  of  $\pm 0.07$ .

would be equivalent to differences in the inferred distance and reddening and possibly difference in the adopted magnitude zero-points.

Using this shifted measurement isochrone, we obtained the best-fitting slope of the mass function  $\alpha_{\text{rec}}$  from the artificial luminosity distribution in the same way as for the observations. We find that over- or underestimating the cluster’s age, metallicity or  $[\alpha/\text{Fe}]$  by 1 Gyr or 0.2 dex respectively, results in systematic offsets between the inserted and measured mass function slope by  $\Delta\alpha = \|\alpha_{\text{rec}} - \alpha_{\text{in}}\| = 0.05 - 0.15$ . The effect of solely the distance uncertainty, estimated by using a measurement isochrone with the same age,  $[\text{Fe}/\text{H}]$  and  $[\alpha/\text{Fe}]$  as the input isochrone, but shifting it by  $\pm 0.04$  mag in distance modulus (corresponding to the distance uncertainty of 1.3 kpc, cf. Section 2.2), yields an offset of  $\Delta\alpha \leq 0.05$ . In the tested range of inserted mass function slopes,  $\alpha_{\text{in}} = 0 - 3$ , the offsets only weakly depend on the slope  $\alpha_{\text{in}}$  itself. Therefore, the amplitude of the change in the mass function slope at different radii of the cluster is largely independent of the adopted stellar population parameters and cluster distance, while the absolute value of the slope may be considered subject to a systematic uncertainty of  $\lesssim 0.15$ .

### 3.4.2 Unresolved binaries

In measuring the mass function, we do not take into account the effect of unresolved binaries that are likely contaminating our main-sequence star sample. As mentioned in the introduction, dynamical constraints allow for a binary fraction of  $f_{\text{bin}} \sim 0.3$  (Sollima et al. 2012) in Pal 14. From the specific frequency of blue stragglers and the total magnitude of the cluster, Beccari et al. (2011) estimated a similar binary fraction of  $f_{\text{bin}} \sim 0.3 - 0.4$ .

To estimate the impact of the presence of binaries that are counted as single stars in our measurement, we drew stellar masses from a power-law distribution with varying slope  $\alpha_{\text{in}}$  in the mass-range  $0.08 - 1 M_{\odot}$ . We randomly paired a fraction of  $f_{\text{bin}}/(1 + f_{\text{bin}})$  of these masses, and for each pair calculated the sum of the fluxes of both components from our adopted isochrone and converted the summed flux back to a mass. This results in a sample of stellar masses, in which a fraction of  $f_{\text{bin}}$  represent the mass that would be inferred for an unresolved binary. We measured the best-fitting mass function slope from the sub-set generated stars/binaries with (apparent) masses in the range  $0.53 - 0.8 M_{\odot}$ . Fig 8 shows the difference of the recovered mass function slope  $\alpha_{\text{rec}}$  and the input mass function slope  $\alpha_{\text{in}}$  as a function  $\alpha_{\text{in}}$  for binary fractions  $f_{\text{bin}} = 0.1, 0.3, 0.5$ , and as an (unrealistic) limiting case,  $f_{\text{bin}} = 1$ . Realistic binary fractions ( $f_{\text{bin}} \lesssim 0.5$ ) result in a relatively small systematic error in the mass function slope,  $|\alpha_{\text{rec}} - \alpha_{\text{in}}| \lesssim 0.07$ . It is interesting to note that in the presence of unresolved binaries, mass functions with intrinsic slopes of  $\alpha_{\text{in}} \sim 0.7$  tend to appear steeper, while mass functions with intrinsic slopes of  $\alpha_{\text{in}} \sim 1.7$  tend to appear flatter. Thus, an observed change in the mass function slope from  $\sim 0.5$  to  $\sim 1.6$  like we see it in Pal 14, might in reality even be somewhat larger than suggested by a measurement that ignores possible binarity. In the case of our data, however, the effect would be much smaller than the statistical uncertainty.

### 3.4.3 Photometric errors

Photometric errors, i.e. statistical uncertainties on measured magnitudes, as well as systematics caused by blending or imperfect subtraction of neighboring stars, directly translate into an error in the inferred mass of a star. To estimate the impact of these errors, we followed a similar procedure: we drew stars from a mass function with  $\alpha_{\text{in}} = 0 - 3$  and converted the masses to magnitudes using the adopted isochrone. For each generated star, we then randomly chose one of the 100 artificial stars (described in Section 2) nearest in terms of inserted F555W magnitude to our generated magnitude. If that artificial star was recovered, we added to our generated magnitude the offset between recovered and inserted magnitude of the artificial star (see Fig. 2). If the artificial was not recovered, we rejected the generated magnitude in order to simulate the same degree of incompleteness as in our observations. We converted the resulting sample of magnitudes back to masses and measured the mass function slope  $\alpha_{\text{rec}}$  in the same mass bins and using the same completeness correction as for the observations. We find that photometric errors make the mass function appear systematically more steep, although the offset  $\alpha_{\text{rec}} - \alpha_{\text{in}}$  is marginal, decreasing slightly from 0.08 for  $\alpha_{\text{in}} = 0$  to 0.03 for  $\alpha_{\text{in}} = 3$ .

Compared to the statistical uncertainties of our measured mass function slopes, this effect is negligible.

## 4 DISCUSSION

We have shown that the mass function in Pal 14 steepens with increasing distance from the center, which suggests that Pal 14 is mass-segregated.

### 4.1 Mass segregation vs. the large extent of the cluster

Sollima et al. (2011) measured a projected half-light radius for Pal 14 of  $r_{hp} = 46 \pm 3$  pc, making Pal 14 the most extended Galactic GC and corresponding to a present-day half-mass relaxation time for Pal 14 of  $\sim 20$  Gyr. As noted before, it is therefore not expected that two-body relaxation processes have established mass segregation in Pal 14, unless the cluster had a shorter relaxation time in the past. Since the half-mass relaxation time-scales with  $r_{hp}^{3/2}$  (Spitzer & Hart 1971), a half-mass relaxation time of a few Gyr would require the cluster to have been more compact by a factor of  $\sim 2$  for most of its lifetime, or even more compact for a shorter duration.

Since the stellar distribution of Pal 14 extends out to more than twice of its Jacobi radius of  $r_J = 170 \pm 10$  pc (Sollima et al. 2011, assuming a circular cluster orbit about the Galaxy), it is plausible that the cluster was indeed more compact in the past, or otherwise it is puzzling how such a diffuse cluster could have survived until the present day in the Galactic tidal field. Alternatively, it may have evolved in a less hostile environment of a satellite galaxy and may have been only recently accreted (Sollima et al. 2011). Çalıřkan et al. (2012) concluded that the element abundance ratios of red giants in Pal 14 are consistent with, but do not require an accretion origin of the GC from a dwarf spheroidal galaxy.

In the latter case, i.e. the cluster was similarly extended, and therefore had a similar relaxation time-scale in the past, the observed mass segregation may be primordial. Several mechanisms that can lead to a primordial, or early, mass segregation in clusters have been proposed. McMillan et al. (2007) propose a scenario, in which young star clusters assemble from less massive clumps that have significantly shorter relaxation time-scales, and which therefore can be already mass-segregated at the time of the cluster assembly. The resulting merged cluster will inherit the mass segregation from its constituents. Olczak et al. (2011) found that early dynamical mass segregation also occurs in clusters without substructure, if they are initially sub-virial and therefore undergo a cold collapse. Another possibility is that mass segregation is created in the star-formation process itself due a more efficient accretion of gas through protostars that reside in the cluster's center, where the density of gas is higher (competitive accretion, see Bonnell et al. 2001a,b).

Primordial mass segregation is observed in several young Galactic (e.g. Sagar et al. 1988; Hillenbrand 1997; Hasan & Hasan 2011) and Magellanic Cloud star clusters (e.g. Fischer et al. 1998; Sirianni et al. 2002). Besides Pal 14, also the globular clusters Pal 5 (Koch et al. 2004), Pal 4 (Frank et al. 2012) and potentially the rich cluster Lindsay 38 in the Small Magellanic Cloud (Glatt et al. 2011)

show mass segregation despite having present-day half-mass relaxation times larger than their ages. Baumgardt et al. (2008) suggested that primordial mass segregation together with a depletion of low-mass stars are required to explain the shallow present-day mass functions of at least some Galactic GCs. As mentioned in the introduction, this was also found by Zonoozi et al. (2011) for Pal 14.

For Pal 4, the observational data resemble our present results for Pal 14. Pal 4's half-mass relaxation time (14 Gyr; Frank et al. 2012), albeit shorter than that of Pal 14, exceeds its age, and yet the cluster shows a flattened mass function, as well as a substantial degree of mass segregation in the mass range of  $0.55 - 0.8 M_{\odot}$ . Zonoozi et al. (2014) presented direct  $N$ -body simulations of Pal 4 to specifically address the question whether or not primordial mass segregation is necessary to reproduce the observations. They studied the evolution over 11 Gyr of different models of GCs on circular orbits, starting with either a Kroupa or an initially flattened IMF, and either with or without primordial mass segregation. They found that the current state of Pal 4 (i.e. its mass function, mass segregation, half light radius and mass) can be reproduced *either* by assuming primordial mass segregation, *or* by assuming an IMF already depleted in low-mass stars, compared to the Kroupa IMF.

Similarly, using collisional  $N$ -body simulations to study Pal 14, Zonoozi et al. (2011) have shown that two-body relaxation alone is insufficient in order to deplete the mass function of low-mass stars and hence to establish the observed mass segregation, if the cluster was born with an initial half-mass radius similar to its present-day value and with a Kroupa IMF. On the other hand, they found that a cluster born initially significantly more compact will not evolve to the present extended shape of Pal 14. This is consistent with Pal 14 being (by a factor of  $\sim 4$ ) more extended than predicted by the mass-radius relation that was found by Gieles et al. (2010). This relation can reproduce the size of the majority of Galactic GCs based on the assumption of initially compact clusters whose expansion during 10 Gyr of evolution is driven by mass loss due to stellar evolution, as well as a central energy source such as hard binaries. Both theoretical results suggest that an initially compact cluster, in which mass segregation would have developed dynamically, cannot have expanded to the observed present size of Pal 14 due to *internal* processes alone.

On the other hand the tidal tails around the cluster show that it is subject to *external* processes even at its current large Galactocentric distance of 66 kpc. Baumgardt et al. (2010) used the ratio of the de-projected half-mass radius  $r_h$  to  $r_J$  to quantify how tidally filling a GC is and found two distinct populations among the Galactic GCs, a tidally under-filling group with  $r_h/r_J < 0.05$  and a tidally filling group with  $0.1 < r_h/r_J < 0.3$ . Using  $r_h = 4/3 \times r_{hp}$  and neglecting mass segregation by equating the half-light to the half-mass radius, yields a ratio  $r_h/r_J = 0.35$  for Pal 14, making it one of the most tidally filling Galactic GCs, second only to Pal 5. The extended structure of Pal 5 was explained by Dehnen et al. (2004) as the result of its expansion due to heating induced by a tidal shock during a recent passage through the Galactic disk. Disk shocks in general dominate the evolution of diffuse clusters in the inner Galactic potential (Gnedin et al. 1999) and a significant fraction ( $\gtrsim 17$  per cent) of the inner halo field stars may have originated

in GCs (Martell et al. 2011). Pal 5 is located at a Galactocentric distance of 18.5 kpc and is believed to be near its apogalacticon (Odenkirchen et al. 2003). Pal 14 has a current Galactocentric distance 3.5 times as large, but its orbit is unknown.

In order for disk shocks to become important, a cluster has to cross the Galactic disk within a Galactocentric radius of about 8 kpc, since disk shocks will be considerably weaker for a cluster crossing the outer disk where the stellar density is much lower (Vesperini & Heggie 1997). In addition, disk crossings will occur less frequently for a cluster on a nearly circular orbit at the Galactocentric distance of Pal 14. So Pal 14 would have to be on an eccentric orbit. In fact, assuming that its current distance of 66 kpc is close to its apogalactic radius,  $R_{apo}$ , Pal 14 would have to be on a highly eccentric orbit with  $\epsilon = (R_{apo} - R_{peri}) / (R_{apo} + R_{peri}) = (66 - 8) / (66 + 8) \approx 0.8$  in order to have a perigalactic radius,  $R_{peri}$ , below 8 kpc. Such high eccentricities would imply severe tidal shocking during pericentre passages, being much more hazardous to the cluster than the disk shocks. Such tidal shocks could in fact temporarily unbind large parts of a cluster like Pal 14, since its Jacobi radius could be significantly smaller than the size of the cluster during a pericentre passage. While moving towards apogalacticon the Jacobi radius of the cluster would grow again and re-capture large parts of the temporarily unbound material (Küpper et al. 2010b).

It is therefore possible that the half-light radius of Pal 14 is significantly overestimated due to unbound stars. In  $N$ -body simulations of GCs on eccentric orbits in external tidal fields, Küpper et al. (2010a) found that beyond  $0.5 r_J$ , the surface density profiles of the clusters can be entirely dominated by unbound stars. Since Pal 14 may not be on a circular orbit and may not currently be at its perigalacticon, the mean Jacobi radius to which the cluster adjusts (Küpper et al. 2010a) may be smaller than the present-day value of  $r_J = 170 \pm 10$  pc. Therefore the distribution of stars attributed to Pal 14 could already be dominated by unbound stars at radii smaller than  $\lesssim 85$  pc, and the half-light radius of the bound body of Pal 14 may be significantly smaller than the estimated half-light radius of 46 pc. In this case, the mystery how the diffuse cluster has survived to the present day has a simple solution: the cluster has *not* survived, and what we observe is an already largely disintegrated stellar system.

## 4.2 Mass segregation vs. the non-concentrated blue straggler population

As noted in the introduction, Beccari et al. (2011), based on a geometrically and photometrically complete catalog, found that the population of 24 BS in Pal 14 is not centrally concentrated compared to 24 HB and 191 selected RGB stars. Other Galactic globular clusters, for which a non-segregated population of BS stars (compared to HB or RGB stars) has been found are NGC 5139 ( $\omega$ Cen; Ferraro et al. 2006), NGC 2419 (Dalessandro et al. 2008), Terzan 8 (Salinas et al. 2012) and Arp 2 (Salinas et al. 2012; Carraro & Seleznev 2011). It is interesting to note that an extragalactic origin has been suggested for all of these GCs: Terzan 8 and Arp 2 are likely associated with the Sgr stream (Da Costa & Armandroff 1995; Law & Majewski 2010).  $\omega$ Cen is com-

monly seen as the remnant nucleus of a former Milky Way satellite galaxy (e.g. Lee et al. 1999; Majewski et al. 2000; Hilker & Richtler 2000; Bekki & Freeman 2003) and a similar scenario is being discussed for NGC 2419, although the case seems less clear for this GC (e.g. van den Bergh & Mackey 2004; Ripepi et al. 2007; Cohen et al. 2010; Brüns & Kroupa 2011; di Criscienzo et al. 2011).

For  $\omega$ Cen, Sollima et al. (2007) found no difference in the luminosity function of stars in fields at 12 and 20 arcmin from the cluster center. There are also no indications for a significantly varying dynamical mass-to-light ratio out to  $\sim 3$  half-light radii (van de Ven et al. 2006; Jalali et al. 2012) and also the velocity dispersion of MS stars as a function of their mass indicates that energy equipartition has not been established in the cluster’s center (Anderson & van der Marel 2010). Also for NGC 2419 there is no evidence for a radially changing luminosity function (Bellazzini et al. 2012). Therefore,  $\omega$ Cen and NGC 2419 can be regarded as not being mass-segregated. For Terzan 8 no further data beyond the comparison of BS and HB and RGB stars by Salinas et al. (2012) are available. In Arp 2, which has the lowest present-day half-mass relaxation time among these GCs (8 Gyr, Salinas et al. 2012), the situation is similar to the situation in Pal 14: Carraro & Seleznev (2011) find that the radial distribution of BS stars is not statistically different from that of HB and RGB stars (although the histogram shown in their fig. 6 may convey the impression of a higher concentration of BS in the innermost radial bin), but MS stars have a more extended radial distribution, indicating that Arp 2 is mass-segregated.

The apparent conflict in clusters like Pal 14 and Arp 2 between a non-concentrated population of BS and a MS population that shows mass segregation may be due to the different time-scales traced by the sinking-in of BS and the depletion of MS stars in the center. The time-scale for mass segregation is shortest for the highest mass stars, turning into the dynamical friction time-scale in the case of masses much larger than the average stellar mass in the cluster. Therefore at some early point in the evolution of a cluster, the highest mass stars, or rather their stellar remnants, will already have sunken to the center, while the intermediate-mass BS still remain largely unaffected by dynamical evolution. The orbital energy lost by the high-mass remnants will deplete the center of, preferentially, low-mass stars, such as those on the main sequence. Indeed, simulations of Pal 4 (Zonoozi et al. 2014) show that on a time-scale of 11 Gyr, which is of the same order of magnitude as Pal 4’s half-mass relaxation time, two-body relaxation processes are sufficient to establish an observable degree of mass segregation among main sequence stars in the mass range  $0.55 - 0.8 M_{\odot}$  – even in GCs, which have low masses and large half-light radii at the present day. In the framework of Ferraro et al. (2012), who classify Galactic GCs into three stages of dynamical evolution based on the radial distribution of BS, Pal 14, together with  $\omega$ Cen and NGC 2419 comprises the dynamically unevolved ‘family 1’ of GCs. Since in contrast to  $\omega$ Cen and NGC 2419, Pal 14 is already depleted of low-mass stars in the center, in this picture, Pal 14 might be on the verge of transitioning towards the dynamically intermediate ‘family 2’.

Finally, we note that in the competitive accretion scenario that was mentioned above in the context of primordial

mass segregation, it is also conceivable that stars are generally segregated by mass, but that the distribution of binaries (such as the BS progenitors) is not necessarily more centrally concentrated, although to our knowledge this has not been studied theoretically yet.

## 5 SUMMARY

Using archival *HST* data we showed that the main-sequence stars of Pal 14 clearly indicate mass segregation in the sense that the cluster is significantly depleted in low-mass stars in its core with respect to larger radii.

The radial dependence of the stellar mass function in Pal 14 was measured using deep archival *V* and *I*-band imaging obtained with the *HST*/WFPC2. We find that in the stellar mass range  $0.53 \leq m \leq 0.80 M_{\odot}$  the stellar mass function is described by a shallow power-law slope of  $\alpha = 0.5 \pm 0.2$  in the cluster’s core, while at larger radii the present-day mass function with a slope of  $\alpha = 1.6 \pm 0.3$  is still below a Kroupa IMF in this mass range ( $\alpha=2.3$ ).

In order for mass segregation in Pal 14 and its overall mass function being depleted of low-mass stars to be the result of two-body relaxation processes, Pal 14 must have been significantly more compact in the past, since its present-day half-mass two-body relaxation time is of the order of 20 Gyr. The expansion of more than a factor of 2 in size may have been caused by severe tidal shocks during pericentre passages on a very eccentric cluster orbit about the Milky Way, as it has been similarly suggested for Palomar 5 with disk shocks (Dehnen et al. 2004).

Alternatively, the cluster might have been given this extended shape by the gas expulsion process at birth which might also be the origin of the depleted mass function (Marks et al. 2008). For such an extended cluster to have survived to the present day, this birth process is likely to have happened in a very remote environment, far away from the destructive tidal forces of the Milky Way.

Hence, Pal 14 could either be an initially compact native Milky Way cluster on a very eccentric orbit, or be a recently accreted globular cluster which formed with primordial mass segregation far away from the Galaxy.

In any case, due to the mass segregation the tidal tails of Pal 14 should show a mass function enriched in low-mass stars, so that mapping their full extent will require deep imaging reaching well below the cluster’s main-sequence turn-off point.

## ACKNOWLEDGMENTS

This work was partially supported by Sonderforschungsbereich 881, ‘The Milky Way System’ (subprojects A2 and A3) of the German Research Foundation (DFG) at the University of Heidelberg.

M.J.F. and A.H.W.K. gratefully acknowledge support from the DFG via Emmy Noether Grant Ko 4161/1 and project KR 1635/28-1, respectively. AHWK would like to acknowledge support through DFG Research Fellowship KU 3109/1-1 and from NASA through Hubble Fellowship grant HST-HF-51323.01-A awarded by the Space Telescope Science Institute, which is operated by the Association of Uni-

versities for Research in Astronomy, Inc., for NASA, under contract NAS 5-26555.

Based on observations made with the NASA/ESA Hubble Space Telescope, obtained from the Multimission Archive at the Space Telescope Science Institute (MAST). STScI is operated by the Association of Universities for Research in Astronomy, Inc., under NASA contract NAS5-26555.

## REFERENCES

- Abazajian K. N. et al., 2009, *ApJS*, 182, 543  
 Anderson J., van der Marel R. P., 2010, *ApJ*, 710, 1032  
 Armandroff T. E., Da Costa G. S., Zinn R., 1992, *AJ*, 104, 164  
 Arp H., van den Bergh S., 1960, *PASP*, 72, 48  
 Baumgardt H., De Marchi G., Kroupa P., 2008, *ApJ*, 685, 247  
 Baumgardt H., Grebel E. K., Kroupa P., 2005, *MNRAS*, 359, L1  
 Baumgardt H., Parmentier G., Gieles M., Vesperini E., 2010, *MNRAS*, 401, 1832  
 Beccari G., Sollima A., Ferraro F. R., Lanzoni B., Bellazzini M., De Marchi G., Valls-Gabaud D., Rood R. T., 2011, *ApJ*, 737, L3  
 Bekki K., Freeman K. C., 2003, *MNRAS*, 346, L11  
 Bellazzini M., Dalessandro E., Sollima A., Ibata R., 2012, *MNRAS*, 423, 844  
 Bonnell I. A., Bate M. R., Clarke C. J., Pringle J. E., 2001a, *MNRAS*, 323, 785  
 Bonnell I. A., Clarke C. J., Bate M. R., Pringle J. E., 2001b, *MNRAS*, 324, 573  
 Brüns R. C., Kroupa P., 2011, *ApJ*, 729, 69  
 Çalışkan Ş., Christlieb N., Grebel E. K., 2012, *A&A*, 537, A83  
 Carraro G., Seleznev A. F., 2011, *MNRAS*, 412, 1361  
 Cohen J. G., Kirby E. N., Simon J. D., Geha M., 2010, *ApJ*, 725, 288  
 Da Costa G. S., Armandroff T. E., 1995, *AJ*, 109, 2533  
 Dalessandro E., Lanzoni B., Ferraro F. R., Vespe F., Bellazzini M., Rood R. T., 2008, *ApJ*, 681, 311  
 Dehnen W., Odenkirchen M., Grebel E. K., Rix H.-W., 2004, *AJ*, 127, 2753  
 di Criscienzo M. et al., 2011, *MNRAS*, 414, 3381  
 Dolphin A. E., 2000, *PASP*, 112, 1383  
 Dotter A., Chaboyer B., Jevremović D., Kostov V., Baron E., Ferguson J. W., 2008a, *ApJS*, 178, 89  
 Dotter A., Sarajedini A., Yang S.-C., 2008b, *AJ*, 136, 1407  
 Ferraro F. R. et al., 2009, *Nature*, 462, 1028  
 Ferraro F. R. et al., 2012, *Nature*, 492, 393  
 Ferraro F. R., Sollima A., Rood R. T., Origlia L., Pancino E., Bellazzini M., 2006, *ApJ*, 638, 433  
 Fischer P., Pryor C., Murray S., Mateo M., Richtler T., 1998, *AJ*, 115, 592  
 Frank M. J., Hilker M., Baumgardt H., Côté P., Grebel E. K., Haggi H., Küpper A. H. W., Djorgovski S. G., 2012, *MNRAS*, 423, 2917  
 Geller A. M., Mathieu R. D., 2011, *Nature*, 478, 356  
 Gentile G., Famaey B., Angus G., Kroupa P., 2010, *A&A*, 509, A97  
 Gieles M., Baumgardt H., Haggie D. C., Lamers H. J. G. L. M., 2010, *MNRAS*, 408, L16  
 Glatt K. et al., 2008, *AJ*, 135, 1106  
 Glatt K. et al., 2011, *AJ*, 142, 36  
 Gnedin O. Y., Lee H. M., Ostriker J. P., 1999, *ApJ*, 522, 935  
 Haggi H., Baumgardt H., Kroupa P., 2011, *A&A*, 527, A33  
 Haggi H., Baumgardt H., Kroupa P., Grebel E. K., Hilker M., Jordi K., 2009, *MNRAS*, 395, 1549  
 Harris W. E., 1996, *AJ*, 112, 1487  
 Hasan P., Hasan S. N., 2011, *MNRAS*, 413, 2345  
 Hilker M., 2006, *A&A*, 448, 171  
 Hilker M., Richtler T., 2000, *A&A*, 362, 895  
 Hillenbrand L. A., 1997, *AJ*, 113, 1733  
 Hills J. G., Day C. A., 1976, *ApL*, 17, 87  
 Holtzman J. A., Afonso C., Dolphin A., 2006, *ApJS*, 166, 534  
 Holtzman J. A., Burrows C. J., Casertano S., Hester J. J., Trauger J. T., Watson A. M., Worthey G., 1995, *PASP*, 107, 1065  
 Hudson D. J., 1971, *J. R. Stat. Soc. B*, 33, pp. 256  
 Jalali B., Baumgardt H., Kissler-Patig M., Gebhardt K., Noyola E., Lützgendorf N., de Zeeuw P. T., 2012, *A&A*, 538, A19  
 Jordi K., Grebel E. K., 2010, *A&A*, 522, A71  
 Jordi K. et al., 2009, *AJ*, 137, 4586  
 Kim Y.-C., Demarque P., Yi S. K., Alexander D. R., 2002, *ApJS*, 143, 499  
 Koch A., Grebel E. K., Odenkirchen M., Martínez-Delgado D., Caldwell J. A. R., 2004, *AJ*, 128, 2274  
 Koekemoer A. M., Fruchter A. S., Hook R. N., Hack W., Hanley C., 2006, in *The 2005 HST Calibration Workshop: Hubble After the Transition to Two-Gyro Mode*, Koekemoer A. M., Goudfrooij P., Dressel L. L., eds., p. 423  
 Kroupa P., 2001, *MNRAS*, 322, 231  
 Kruijssen J. M. D., Mieske S., 2009, *A&A*, 500, 785  
 Küpper A. H. W., Kroupa P., 2010, *ApJ*, 716, 776  
 Küpper A. H. W., Kroupa P., Baumgardt H., Haggie D. C., 2010a, *MNRAS*, 407, 2241  
 Küpper A. H. W., Kroupa P., Baumgardt H., Haggie D. C., 2010b, *MNRAS*, 401, 105  
 Küpper A. H. W., Mieske S., Kroupa P., 2011, *MNRAS*, 413, 863  
 Lanzoni B., Dalessandro E., Ferraro F. R., Mancini C., Beccari G., Rood R. T., Mapelli M., Sigurdsson S., 2007, *ApJ*, 663, 267  
 Law D. R., Majewski S. R., 2010, *ApJ*, 718, 1128  
 Lee Y.-W., Joo J.-M., Sohn Y.-J., Rey S.-C., Lee H.-C., Walker A. R., 1999, *Nature*, 402, 55  
 Majewski S. R., Patterson R. J., Dinescu D. I., Johnson W. Y., Ostheimer J. C., Kunkel W. E., Palma C., 2000, in *Liege International Astrophysical Colloquia*, Noels A., Magain P., Caro D., Jehin E., Parmentier G., Thoul A. A., eds., Vol. 35, p. 619  
 Mapelli M., Sigurdsson S., Ferraro F. R., Colpi M., Possenti A., Lanzoni B., 2006, *MNRAS*, 373, 361  
 Marigo P., Girardi L., Bressan A., Groenewegen M. A. T., Silva L., Granato G. L., 2008, *A&A*, 482, 883  
 Marín-Franch A. et al., 2009, *ApJ*, 694, 1498  
 Marks M., Kroupa P., Baumgardt H., 2008, *MNRAS*, 386, 2047  
 Martell S. L., Smolinski J. P., Beers T. C., Grebel E. K.,

- 2011, *A&A*, 534, A136
- McCrea W. H., 1964, *MNRAS*, 128, 147
- McMillan S. L. W., Vesperini E., Portegies Zwart S. F., 2007, *ApJ*, 655, L45
- Mighell K. J., 1999, *ApJ*, 518, 380
- Milgrom M., 1983, *ApJ*, 270, 371
- Odenkirchen M. et al., 2003, *AJ*, 126, 2385
- Olczak C., Spurzem R., Henning T., 2011, in *IAU Symposium*, Brummell N. H., Brun A. S., Miesch M. S., Ponty Y., eds., Vol. 271, pp. 389–390
- Ripepi V. et al., 2007, *ApJ*, 667, L61
- Robin A. C., Reyl e C., Derri ere S., Picaud S., 2003, *A&A*, 409, 523
- Rust R. T., Simester D., Brodie R. J., Nilikant V., 1995, *Management Science*, 41, pp. 322
- Sagar R., Miakutin V. I., Piskunov A. E., Dluzhnevskaja O. B., 1988, *MNRAS*, 234, 831
- Salinas R., J ilkova L., Carraro G., Catelan M., Amigo P., 2012, *MNRAS*, 421, 960
- Salpeter E. E., 1955, *ApJ*, 121, 161
- Sarajedini A., 1997, *AJ*, 113, 682
- Shara M. M., Saffer R. A., Livio M., 1997, *ApJ*, 489, L59
- Sirianni M., Nota A., De Marchi G., Leitherer C., Clampin M., 2002, *ApJ*, 579, 275
- Sollima A., Ferraro F. R., Bellazzini M., 2007, *MNRAS*, 381, 1575
- Sollima A., Mart inez-Delgado D., Valls-Gabaud D., Pe arrubia J., 2011, *ApJ*, 726, 47
- Sollima A., Nipoti C., 2010, *MNRAS*, 401, 131
- Sollima A., Nipoti C., Mastrobuono Battisti A., Montuori M., Capuzzo-Dolcetta R., 2012, *ApJ*, 744, 196
- Spitzer, Jr. L., 1969, *ApJ*, 158, L139
- Spitzer, Jr. L., Hart M. H., 1971, *ApJ*, 164, 399
- Stetson P. B., 2000, *PASP*, 112, 925
- van de Ven G., van den Bosch R. C. E., Verolme E. K., de Zeeuw P. T., 2006, *A&A*, 445, 513
- van den Bergh S., Mackey A. D., 2004, *MNRAS*, 354, 713
- Vesperini E., Heggie D. C., 1997, *MNRAS*, 289, 898
- Zinn R., 1985, *ApJ*, 293, 424
- Zonoozi A. H., Haghi H., K upper A. H. W., Baumgardt H., Frank M. J., Kroupa P., 2014, *MNRAS*, 440, 3172
- Zonoozi A. H., K upper A. H. W., Baumgardt H., Haghi H., Kroupa P., Hilker M., 2011, *MNRAS*, 411, 1989

This paper has been typeset from a  $\text{\LaTeX}$  file prepared by the author.